



Synthesis of one-dimensional Bi_2O_3 - $\text{Bi}_2\text{O}_{2.33}$ heterojunctions with high interface quality for enhanced visible light photocatalysis in degradation of high-concentration phenol and MO dyes

Yin Peng ^{a,b,*,} Ke Ke Wang ^a, Ting Liu ^a, Jian Xu ^a, Bin Gang Xu ^{b,*}

^a The Key Laboratory of Functional Molecular Solids, Ministry of Education, College of Chemistry and Materials Science, Anhui Normal University, Wuhu 241000, China

^b Nanotechnology Center, Institute of Textiles and Clothing, The Hong Kong Polytechnic University, Hung Hom, Kowloon, Hong Kong

ARTICLE INFO

Article history:

Received 10 July 2016

Received in revised form 2 November 2016

Accepted 8 November 2016

Available online 9 November 2016

Keywords:

Photocatalysis

Environmental remediation

Interface quality

Bi_2O_3 - $\text{Bi}_2\text{O}_{2.33}$ heterostructure

ABSTRACT

One-dimensional (1D) Bi_2O_3 - $\text{Bi}_2\text{O}_{2.33}$ heterostructures were synthesized by calcining $\text{Bi}_2\text{O}_2\text{CO}_3$ - $\text{Bi}(\text{OHC}_2\text{O}_4)\cdot 2\text{H}_2\text{O}$ precursors. Ultrathin $\text{Bi}_2\text{O}_{2.33}$ nanosheets were uniformly patched onto the porous Bi_2O_3 rod with well-matched lattice fringes, which increased the interface quality and then provided the smallest penetration barrier for electron-hole pairs transfer between Bi_2O_3 - $\text{Bi}_2\text{O}_{2.33}$ interfaces. The photocatalytic performance of the obtained products was evaluated by the degradation of high-concentration methyl orange (MO) and phenol under solar/visible light irradiation. The results show that Bi_2O_3 - $\text{Bi}_2\text{O}_{2.33}$ heterostructure displays higher photocatalytic activity than pure phase Bi_2O_3 and $\text{Bi}_2\text{O}_{2.33}$, and more encouragingly, 30 mg/L of MO (or phenol) can be completely degraded in 60 min under visible light irradiation using Bi_2O_3 - $\text{Bi}_2\text{O}_{2.33}$ (S2) heterostructure as photocatalyst. This enhanced photocatalytic performance is ascribed to the synergistic effect of the suitable band alignment of the Bi_2O_3 and $\text{Bi}_2\text{O}_{2.33}$, high interface quality between Bi_2O_3 and $\text{Bi}_2\text{O}_{2.33}$ junctions and one-dimensional ordered nanostructure. This work would offer a novel route to design and fabrication of junction structures with high interface quality for photocatalytic applications.

© 2016 Elsevier B.V. All rights reserved.

1. Introduction

Environmental and energy issues are one of the biggest global challenges we are facing in the new century. With the rapid growth of worldwide industry, severe environmental contaminations have become a major concern of our society. Therefore, development of high efficient, green energy sources and eco-friendly methods for environmental remediation is highly in demand. As one of the promising technologies, photocatalysis which utilizes solar energy to solve environmental and energy issues has attracted considerable attention.

To be a good photocatalyst, the candidate should be not only efficient in absorbing solar light, but also effective in de-

creasing the recombination of the photogenerated carriers before they reach surface reaction sites. This is always crucial for efficient energy conversion (from solar to chemical) and for photodecomposition of organic molecules. In the past decades, a great deal of effort has been made towards the good photocatalyst, and the notable ones include formation of semiconductor heterostructures, co-deposition of noble metals, doping, surface hybridization and incorporation with other technologies. Among these approaches, formation of semiconductor heterostructures is one of most effective strategies to balance the harsh terms because of the tuneable band structures and efficient electron-hole separation and transportation, which endows them with suitable properties superior to their individual components [1–3].

For heterostructural photocatalysts, interface quality is extremely important for enhancing photocatalytic activity because charge transfer between semiconductor interfaces is finished within picoseconds, and this fast transfer rate requires the smallest penetration barrier in the interface [4,5]. A difference in lattice spacing between two semiconductors likely causes lattice mismatch. A large lattice mismatch at the interface may cause defects which trap the photogenerated carriers and thus

* Corresponding author at: Nanotechnology Center, Institute of Textiles and Clothing, The Hong Kong Polytechnic University, Hung Hom, Kowloon, Hong Kong.

** Corresponding author at: The Key Laboratory of Functional Molecular Solids, Ministry of Education, College of Chemistry and Materials Science, Anhui Normal University, Wuhu 241000, China.

E-mail addresses: kimipeng@mail.ahnu.edu.cn (Y. Peng), tcxubg@polyu.edu.hk (B.G. Xu).

prevent the diffusion of electrons and holes. In addition, large lattice mismatch will also result in chemically weak bonds and high penetration barrier at interface, which is responsible for the instability of the heterojunction photocatalyst. Therefore, low interfacial defects and chemically strong bonds across the interface with large contact areas (namely interface with small lattice mismatch) are preferred for eliminating the penetration barrier in the interface [6–12].

Over the past decade, fabrication of a high interface quality in heterostructured catalysts has attracted a growing attention worldwide [10–19]. According to the reported results, it is believed that the similar composition on both sides of the interface can provide continuity of the bonding across the heterostructural boundary, which may facilitate the charge transfer across the interface. For example: ATiO_3 (A: Pb, Fe)/ TiO_2 had a higher reactivity for photodecomposition of methylene blue than AFeO_3 (A: Bi, La, Y)/ TiO_2 at the same conditions [19]. The reason is that the Ti-O-Ti chemically strong bonds can be formed between ATiO_3 and TiO_2 at the interface instead of AFeO_3 and TiO_2 . $\text{Sr}_2\text{TiO}_4/\text{SrTiO}_3$ (La, Cr) heterojunction photocatalyst shows higher photocatalytic activity towards hydrogen production than individual SrTiO_3 (La, Cr) and Sr_2TiO_4 (La, Cr) [10]. Microscopic morphology studies show that well defined heterojunctions are formed by matching the lattice fringes of SrTiO_3 (La, Cr) and Sr_2TiO_4 (La, Cr). Formation of this well matched heterojunction is expected to facilitate charge transfer and separation between the nanoparticles, thereby enhancing the photocatalytic activity [20–22].

A junction can also be formed between two different polymorphs of phases with exactly the same composition (called homostructure) [11,12,23–27]. Compared with heterojunctions made of two different compositions, the same component on both sides of the homojunction interface renders continuity of the band bonding and promotes the transfer of photoexcited charge carriers across the interface. For example: a- Ga_2O_3 /b- Ga_2O_3 junctions with well matched lattice fringes were obtained through a phase transformation from a- Ga_2O_3 at elevated temperature, which showed much higher photocatalytic activity for water splitting under UV-light irradiation than the pure a or b phases [11]. A new, crystal facet-based CeO_2 homojunction was synthesized through solution-based crystallographic oriented epitaxial growth. This homostructural interface with completely matched lattice fringes provides convenient and fast channels for the photogenerated carrier transportation between two units of homojunction [12]. Inspired by the above conclusions, we design and synthesize bismuth oxide (Bi_2O_3) heterostructure with the same composition on both sides of the interface.

Bi_2O_3 has attracted great interest in photocatalytic areas owing to its low cost, nontoxicity, and relatively narrow band gap and higher oxidation power of the valence holes properties. Besides extensive five main crystalline phases of Bi_2O_3 , there are also two nonstoichiometric phases including $\text{Bi}_2\text{O}_{2.75}$ and $\text{Bi}_2\text{O}_{2.33}$ [28]. Up to now, most of the work on bismuth oxides has focused on Bi_2O_3 , while there have been only a few reports on $\text{Bi}_2\text{O}_{2.33}$ [29–33]. These few reports have shown that the nonstoichiometric phase $\text{Bi}_2\text{O}_{2.33}$ is a good functional semiconductor with UV light emitters [29], high performance supercapacitor [30], room-temperature ferromagnetic semiconductor [31], photocatalyst for degrading RhB dye [32] and efficient iodine adsorbent [33]. However, there is no report on the synthesis and photocatalytic performance of $\text{Bi}_2\text{O}_{2.33}$ heterostructure.

In this work, we first synthesized one-dimensional Bi_2O_3 - $\text{Bi}_2\text{O}_{2.33}$ heterostructures with well matched lattice fringes by high temperature calcining $\text{Bi}_2\text{O}_2\text{CO}_3$ - $\text{Bi}(\text{OHC}_2\text{O}_4)\cdot 2\text{H}_2\text{O}$ precursors. Methylene orange (MO) and phenol were used as model compounds to investigate the photocatalytic activities of the Bi_2O_3 - $\text{Bi}_2\text{O}_{2.33}$ heterostructure under solar/visible light irradiation. The

results demonstrated that the Bi_2O_3 - $\text{Bi}_2\text{O}_{2.33}$ photocatalyst is highly efficient for degradation of high-concentration phenol and MO dyes, and the S2 sample shows an excellent photocatalytic activity as compared to the recently reported Bi-based photocatalysts under the similar conditions [34–48]. The enhanced photocatalytic performance is attributed to a synergistic effect of the following three factors: (1) suitable band alignment of the Bi_2O_3 and $\text{Bi}_2\text{O}_{2.33}$ drives electrons and holes to reach the most stable energy configuration and then leads to a spatial charge separation; (2) the interfaces with well matched lattice fringe provide small penetration barrier for the photogenerated carriers transfer across the Bi_2O_3 - $\text{Bi}_2\text{O}_{2.33}$ heterojunctions; and (3) one-dimensional ordered nanostructure is desirable for facilitating high efficient and directional transport and separation of electrons and holes. This work provided a novel route to synthesize advanced materials with high interface quality for photocatalytic applications.

2. Experimental section

2.1. Sample preparation

All reagents were analytical grade and used without any further purification in our experiment.

$\text{Bi}_2\text{O}_2\text{CO}_3$ - $\text{Bi}(\text{OHC}_2\text{O}_4)\cdot 2\text{H}_2\text{O}$ precursors were synthesized according to our early report [49]. In the typical synthesis, $\text{Bi}(\text{OHC}_2\text{O}_4)\cdot 2\text{H}_2\text{O}$ nanorods (0.5 mmol), CTAB (0.5 g) and a certain amounts of Na_2CO_3 were dispersed into distilled water (40 mL) under magnetic stirring for 30 min, and then a certain amount of $\text{Bi}(\text{NO}_3)_3\cdot 5\text{H}_2\text{O}$ were added with constant stirring for 2 h to obtain samples. The products were washed several times with distilled water and anhydrous ethanol, and then dried in air at 60 °C for 4 h. The as-obtained precursors were labelled as PS1–PS4 when the molar ratio of $\text{Bi}(\text{OHC}_2\text{O}_4)\cdot 2\text{H}_2\text{O}$: $\text{Bi}(\text{NO}_3)_3\cdot 5\text{H}_2\text{O}$ were 20:1, 20:2, 20:3 and 20:4, respectively.

Then, Bi_2O_3 - $\text{Bi}_2\text{O}_{2.33}$ samples were obtained by calcining $\text{Bi}_2\text{O}_2\text{CO}_3$ - $\text{Bi}(\text{OHC}_2\text{O}_4)\cdot 2\text{H}_2\text{O}$ precursors at 350 °C for 3 h in air, and the respective calcined products were labeled as S1–S4, respectively.

Bi_2O_3 were obtained by calcining $\text{Bi}(\text{OHC}_2\text{O}_4)\cdot 2\text{H}_2\text{O}$ at 350 °C for 3 h in air.

2.2. Test of photocatalytic activity

Photocatalytic activity of the prepared Bi_2O_3 - $\text{Bi}_2\text{O}_{2.33}$ samples was evaluated by decomposing phenol and MO dyes under solar/visible light irradiation. The light source was a 500 W Xe lamp (PLS-SXE500/500UV, Trusttech Co., Ltd. Beijing) with a 400 nm UV cutoff filter. The reaction was maintained at room temperature by a cooling water circulation. In a typical photocatalytic experiment, 100 mg photocatalyst was dispersed in 100 mL 30 mg/L of MO (or phenol) solution under magnetic stirring for 30 min in dark to reach an adsorption-desorption equilibrium between MO (or phenol) and the photocatalyst before irradiation. Then, the suspension was illuminated by the Xe lamp combined with a UV cutoff filter ($\lambda \geq 400$ nm) under magnetic stirring. At given time intervals, above 3 mL suspension was withdrawn, and centrifuged to remove the precipitate. The degradation reaction process was monitored by measuring the concentration of MO (or phenol) as a function of irradiation time in the solution with UV-vis absorption spectrum. Additionally, the recycling experiments were performed for five consecutive cycles to test the durability. After each cycle, the photocatalyst was centrifuged and used directly for the next test.

The experiments of trapping active species are similar to the photocatalytic tests. Scavengers *t*-butanol, *p*-benzoquinone (BQ) and ammonium oxalate (AO) were added into MO solution to trap

hydroxyl radicals ($\cdot\text{OH}$), the superoxide radicals ($\cdot\text{O}_2^-$) and hole (h^+), respectively, followed by the photocatalytic tests.

All the photocatalytic experiments in this article were carried out at neutral pH.

2.3. Characterization

Field emission scanning electron microscopy (FE-SEM) images were recorded on a Hitachi S-4800 microscope. Transmission electron microscopic (TEM) images and high-resolution transmission electron microscopic (HRTEM) images were performed on a JEOL-2010 microscope with an accelerating voltage of 200 kV. X-Ray powder diffraction (XRD) was carried out on a Rigaku (Japan) D/max γA X-ray diffractometer with Cu-K α radiation ($\lambda = 0.154178 \text{ nm}$). UV-vis diffuse-reflectance spectrum was recorded with a UV-2450 spectrophotometer in the wavelength range of 200–800 nm at room temperature. BaSO_4 was used as the reflectance standard material. The X-Ray photoelectron spectroscopy (XPS) was performed on a Perkin-Elmer RBD upgraded PHI-5000C ESCA system. Nitrogen adsorption–desorption measurements were performed at 77 K using a Micromeritics Tristar II 3020 M analyzer after the samples were degassed at 180 °C for 6 h. The Brunauer–Emmett–Teller (BET) surface area was estimated by using adsorption data. The thermal stability was investigated by a thermogravimetric-differential thermal analyzer (TG-DTA, TGA/DSC 1, Mettler Toledo) in an air atmosphere. Total organic carbon (TOC) analyzer (Multi N/C 2100, Jena) was employed for mineralization degree analysis of phenol and MO solution.

3. Results and discussion

3.1. Structure and morphology of photocatalysts

The XRD patterns of $\text{Bi}_2\text{O}_2\text{CO}_3\text{-Bi}(\text{OHC}_2\text{O}_4)\text{-2H}_2\text{O}$ precursors have been reported in reference 49. Calcine $\text{Bi}_2\text{O}_2\text{CO}_3\text{-Bi}(\text{OHC}_2\text{O}_4)\text{-2H}_2\text{O}$ precursors at 350 °C for 3 h in air and obtain the

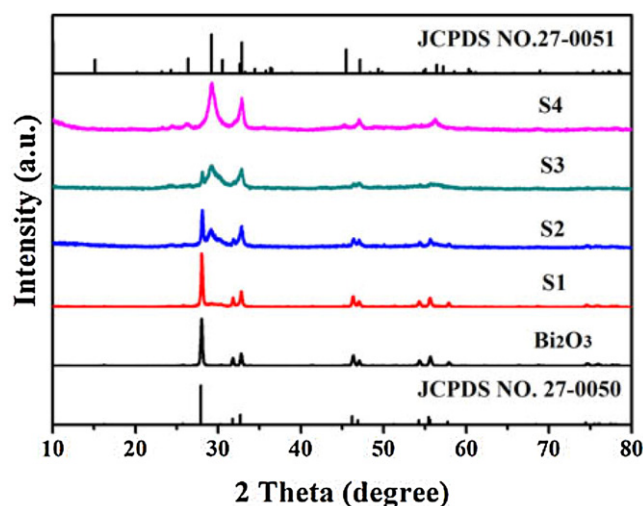


Fig. 1. The XRD patterns of Bi_2O_3 nanorods, $\text{Bi}_2\text{O}_3\text{-Bi}_2\text{O}_{2.33}$ heterojunctions ($\text{S}1 \rightarrow \text{S}4$) and Standard Card of $\text{Bi}_2\text{O}_{2.33}$.

respective calcined-products which were labelled S1–S4, respectively. Fig. 1 gives out their XRD patterns. It was observed that the calcined-product of $\text{Bi}(\text{OHC}_2\text{O}_4)\text{-2H}_2\text{O}$ could be well indexed to tetragonal Bi_2O_3 (JCPDS No. 27-0050). With the increase of loaded- $\text{Bi}_2\text{O}_2\text{CO}_3$ content in the $\text{Bi}_2\text{O}_2\text{CO}_3\text{-Bi}(\text{OHC}_2\text{O}_4)\text{-2H}_2\text{O}$ precursor, the new characteristic diffraction peaks appear and their intensities increase gradually ($\text{S}1 \rightarrow \text{S}4$ samples), which are attributed to tetragonal phase $\text{Bi}_2\text{O}_{2.33}$ (JCPDS No. 27-0051). No additional impurity phase was found in the diffraction pattern, implying the formation of $\text{Bi}_2\text{O}_3\text{-Bi}_2\text{O}_{2.33}$ heterostructures. Moreover, it can be found that only few Bi_2O_3 exists in the S4 sample and the main component is $\text{Bi}_2\text{O}_{2.33}$. So, S4 sample is considered as pure $\text{Bi}_2\text{O}_{2.33}$.

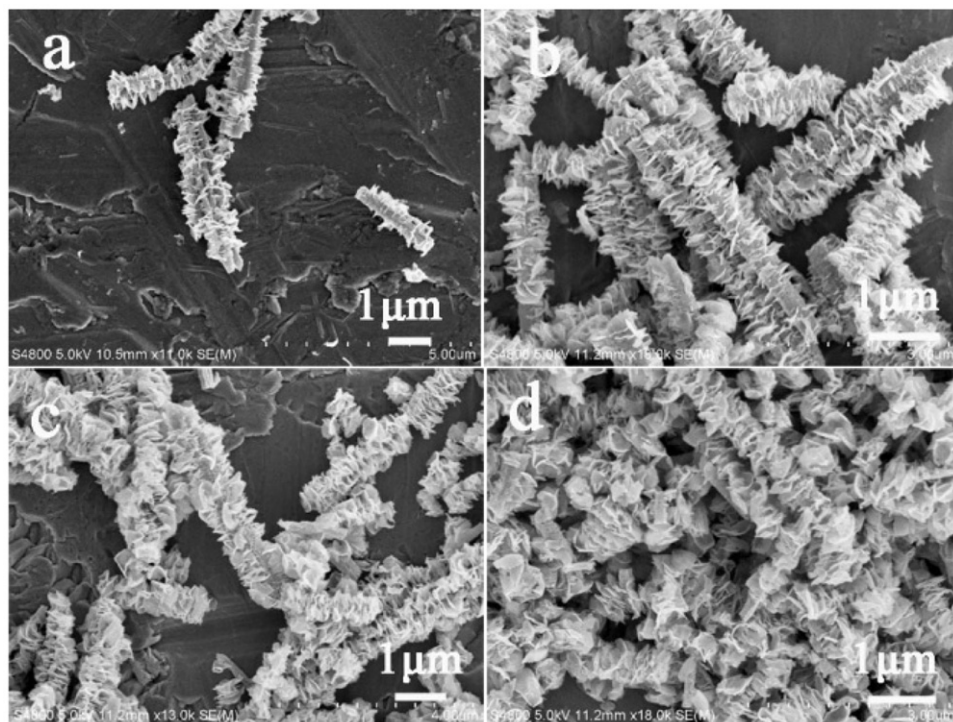


Fig. 2. FE-SEM images of (a) S1, (b) S2, (c) S3 and (d) $\text{Bi}_2\text{O}_{2.33}$.

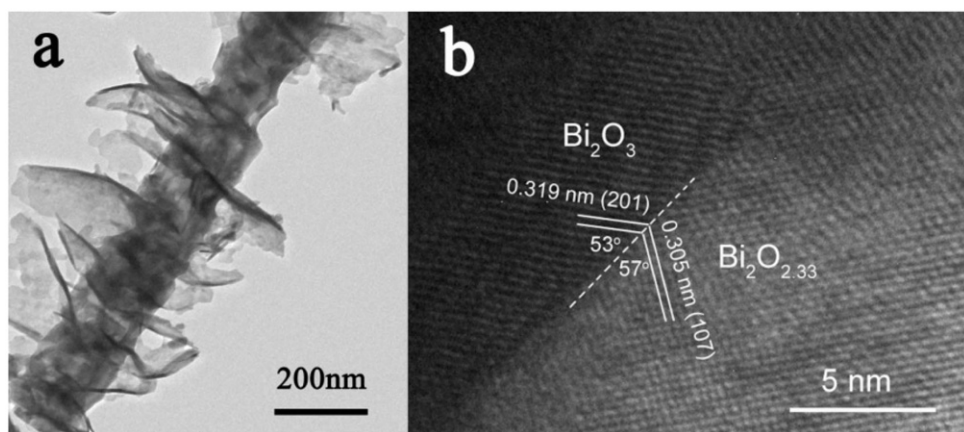


Fig. 3. (a) The TEM and (b) HRTEM images of the S2 heterojunction.

The SEM image of the Bi_2O_3 obtained from calcining $\text{Bi}(\text{OHC}_2\text{O}_4)\cdot 2\text{H}_2\text{O}$ rods at 350°C for 3 h was shown in Fig. S1. It can be seen that the obtained Bi_2O_3 possesses rod-like structure with porosity due to gas removal. The SEM images of the respective calcined-products S1–S3 and $\text{Bi}_2\text{O}_{2.33}$ were shown in Fig. 2. It can be seen that as-made samples keep the original precursor shape without obvious structural collapses [49]. Ultrathin $\text{Bi}_2\text{O}_{2.33}$ nanosheets grow approximately along the radial direction of Bi_2O_3 porous rod, which can also be well observed by TEM in Fig. 3.

TEM technology was used to obtain structural information of the obtained S2 sample in detail. The TEM and HRTEM images of S2 were shown in Fig. 3. It is clearly noted that the $\text{Bi}_2\text{O}_{2.33}$ nanosheets vertically grow onto the surface of the Bi_2O_3 rod, which is consistent with the SEM result. It is also observed that these $\text{Bi}_2\text{O}_{2.33}$ ultrathin nanosheets have many pores due to the CO_2 gas removal from the $\text{Bi}_2\text{O}_2\text{CO}_3$ nanosheets during the calcining process. Fig. 3b displays HRTEM image of the S2 heterojunction. From Fig. 3b it can be clearly seen the interface with well matched lattice fringe between Bi_2O_3 and $\text{Bi}_2\text{O}_{2.33}$ is formed. Clear lattice fringe with a d-spacing of 0.305 nm is ascribed to (107) crystal plane of tetragonal phase $\text{Bi}_2\text{O}_{2.33}$, and the crystal fringe spacing of 0.319 nm corresponds to (201) crystal plane of tetragonal phase Bi_2O_3 . The phase junction between Bi_2O_3 and $\text{Bi}_2\text{O}_{2.33}$ is composed of well-matched lattice fringes between the (201) plane of Bi_2O_3 and the (107) plane of $\text{Bi}_2\text{O}_{2.33}$ with a small interfacial lattice mismatch (m) of 9%, implying high interface quality in $\text{Bi}_2\text{O}_3\text{-Bi}_2\text{O}_{2.33}$ heterostructure. According to above results, it is expected that $\text{Bi}_2\text{O}_3\text{-Bi}_2\text{O}_{2.33}$ heterostructure will display strong ability for photogenerated charge carriers transfer and separation.

XPS measurement was performed to investigate the chemical state of elements. Fig. 4 shows the high resolution Bi 4f XPS spectra of the obtained S2, Bi_2O_3 and $\text{Bi}_2\text{O}_{2.33}$ samples. The peaks located at 163.99 and 158.68 eV are ascribed to $\text{Bi} 4f_{5/2}$ and $\text{Bi} 4f_{7/2}$, respectively, which proves that Bi ions in Bi_2O_3 sample are in form of Bi^{3+} . Compared with the Bi_2O_3 sample, except for the Bi 4f peaks of Bi^{3+} ions, the new peaks located at 161.97 and 156.69 eV are found in the Bi 4f XPS spectra of $\text{Bi}_2\text{O}_{2.33}$ sample. According to early reports [31,33], these peaks are attributed to Bi^{2+} ions. According to the charge balance, there should be two kinds of bismuth ions (Bi^{3+} and Bi^{2+}) in the $\text{Bi}_2\text{O}_{2.33}$ crystal. In the high resolution Bi 4f XPS spectra of S2, the Bi 4f peaks of Bi^{3+} and Bi^{2+} ions appeared simultaneously. Moreover, the peaks of Bi 4f obviously shift to the higher binding energies, as compared to Bi_2O_3 and $\text{Bi}_2\text{O}_{2.33}$. This result indicates that there exists the strong interaction between Bi_2O_3 and $\text{Bi}_2\text{O}_{2.33}$ phases. In addition, the intensity of Bi 4f peaks in S2 is obviously weaker than in $\text{Bi}_2\text{O}_{2.33}$.

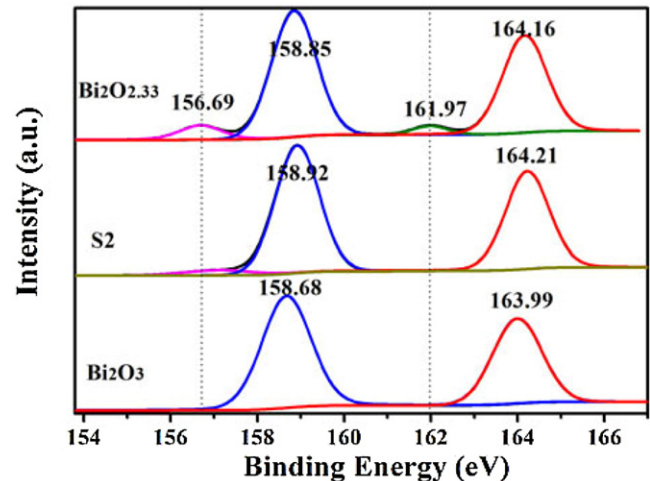


Fig. 4. High-resolution Bi 4f XPS spectra of Bi_2O_3 , $\text{Bi}_2\text{O}_{2.33}$ and S2 samples.

3.2. N_2 adsorption-desorption isotherms and thermogravimetric (TG) analysis

Adsorption and desorption experiments using N_2 were carried out at 77K . Fig. S2a displays the N_2 sorption isotherms of the $\text{Bi}_2\text{O}_3\text{-Bi}_2\text{O}_{2.33}$ heterostructures (S2 sample), pure Bi_2O_3 and $\text{Bi}_2\text{O}_{2.33}$ samples. The shape of the isotherm is a type IV isotherm with a type H3 hysteresis loop at high relative pressures according to the IUPAC classification, which indicates that these samples are mesoporous structures in the pore diameter range of $2\text{--}50\text{ nm}$. This result can be further confirmed by the corresponding pore-size distribution, as shown in Fig. S2b. Considering the observed morphology of the samples, the pores ($20\text{--}25\text{ nm}$) can be generated during thermal treatment process. The BET surface area of the S2 ($14.018\text{ m}^2\text{g}^{-1}$) is higher than that of the pure Bi_2O_3 ($5.672\text{ m}^2\text{g}^{-1}$) and $\text{Bi}_2\text{O}_{2.33}$ ($6.654\text{ m}^2\text{g}^{-1}$). We also find that S2 and pure Bi_2O_3 own larger BET surface areas than their relative precursors, but in reverse for $\text{Bi}_2\text{O}_{2.33}$ [49].

It is well known, when Na_2CO_3 is added into the solution containing $\text{Bi}(\text{OHC}_2\text{O}_4)\cdot 2\text{H}_2\text{O}$ nanorods, CO_3^{2-} ions are first adsorbed on the surface of $\text{Bi}(\text{OHC}_2\text{O}_4)\cdot 2\text{H}_2\text{O}$ nanorods. When $\text{Bi}(\text{NO}_3)_3$ is added into the reaction system, the acid condition is formed due to the Bi^{3+} hydrolysis. And then the Bi^{3+} hydrolysis product will react with CO_3^{2-} in solution to form $\text{Bi}_2\text{O}_2\text{CO}_3$ on the surface of $\text{Bi}(\text{OHC}_2\text{O}_4)\cdot 2\text{H}_2\text{O}$ nanorods. Meanwhile, the preferred outward

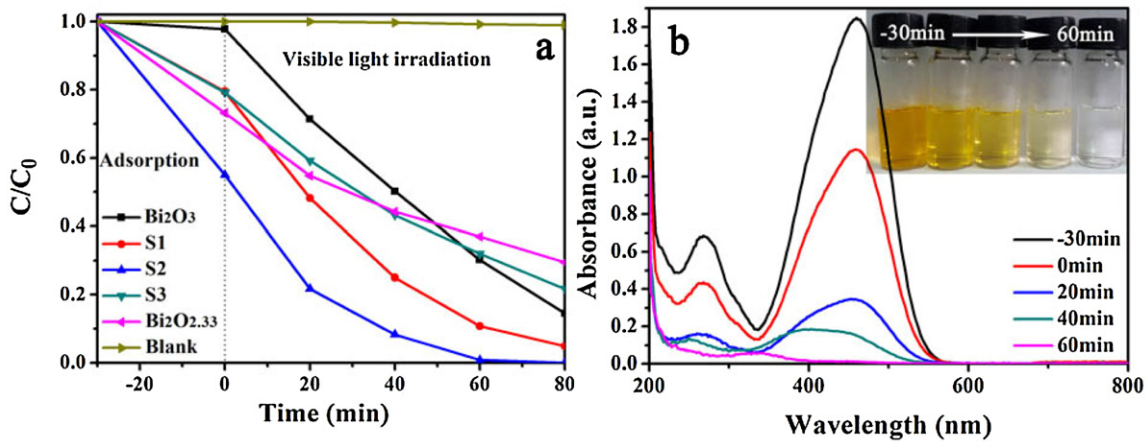


Fig. 5. (a) The degradation curves of MO (30 mg/L) using different photocatalysts and (b) UV-vis absorption spectra of MO (30 mg/L) using S2 as photocatalyst under visible light irradiation.

diffusion of Bi^{3+} ions from $\text{Bi}(\text{OHC}_2\text{O}_4)\cdot 2\text{H}_2\text{O}$ nanorods under acidic conditions reacts with adsorbed CO_3^{2-} ions to form $\text{Bi}_2\text{O}_2\text{CO}_3$, which leads to a net material flux across the composite interface due to the Kirkendall effect. Therefore, $\text{Bi}(\text{OHC}_2\text{O}_4)\cdot 2\text{H}_2\text{O}$ rods were gradually consumed with the increase of the molar ratio of $\text{Bi}(\text{OHC}_2\text{O}_4)\cdot 2\text{H}_2\text{O}$: $\text{Bi}(\text{NO}_3)_3$ (20:1 \rightarrow 20:4). When the molar ratio of $\text{Bi}(\text{OHC}_2\text{O}_4)\cdot 2\text{H}_2\text{O}$: $\text{Bi}(\text{NO}_3)_3$ is more than 20:5, $\text{Bi}(\text{OHC}_2\text{O}_4)\cdot 2\text{H}_2\text{O}$ rods were consumed completely [49]. So, the actual molar ratio of $\text{Bi}(\text{OHC}_2\text{O}_4)\cdot 2\text{H}_2\text{O}$: $\text{Bi}_2\text{O}_2\text{CO}_3$ in the obtained $\text{Bi}(\text{OHC}_2\text{O}_4)\cdot 2\text{H}_2\text{O}$ - $\text{Bi}_2\text{O}_2\text{CO}_3$ precursor is smaller than calculated value (20:1/2, 20:2/2, 20:3/2 and 20:4/2) based on the molar ratio of $\text{Bi}(\text{OHC}_2\text{O}_4)\cdot 2\text{H}_2\text{O}$: $\text{Bi}(\text{NO}_3)_3$. In order to prove above result, Thermogravimetric (TG) curves of $\text{Bi}(\text{OHC}_2\text{O}_4)\cdot 2\text{H}_2\text{O}$ and the precursors (PS1, PS3, PS4) of S1, S3 and S4 were measured. As shown in Fig. S3, the weight losses below 150 °C are mainly attributed to the evaporation of bounded water, while those in the range of 150–500 °C are ascribed to the decomposition of $\text{Bi}_2\text{O}_2\text{CO}_3$ and $\text{Bi}(\text{OHC}_2\text{O}_4)\cdot 2\text{H}_2\text{O}$. Theoretically, the weight losses of $\text{Bi}_2\text{O}_2\text{CO}_3$ and $\text{Bi}(\text{OHC}_2\text{O}_4)\cdot 2\text{H}_2\text{O}$ are 8.6% and 28.28%, respectively. It can be seen from Fig. S3, the weight loss of $\text{Bi}(\text{OHC}_2\text{O}_4)\cdot 2\text{H}_2\text{O}$ is 25.98% in the range 194.12–420.71 °C, which is close to the theoretical value. According to this value and theoretical weight loss value of $\text{Bi}_2\text{O}_2\text{CO}_3$ (8.6%), we roughly calculated the actual molar ratio of $\text{Bi}(\text{OHC}_2\text{O}_4)\cdot 2\text{H}_2\text{O}$: $\text{Bi}_2\text{O}_2\text{CO}_3$ in the PS1, PS3 and PS4 precursors, which is 7:1, 2:1 and 0.3:1, respectively. The relative molar ratio of Bi_2O_3 : $\text{Bi}_{2.33}$ in the calcined products S1, S3 and S4 is 7/2:1, 2/2:1 and 0.3/2:1, respectively.

At present, amounts of works have been reported for the calcined products of $\text{Bi}_2\text{O}_2\text{CO}_3$ at different calcining temperatures. However, $\text{Bi}_{2.33}$ as calcined products of $\text{Bi}_2\text{O}_2\text{CO}_3$ has never been reported. Recently, Zhou et al. synthesized β - Bi_2O_3 nanosheets exposed with active {001} facets through annealing $\text{Bi}_2\text{O}_2\text{CO}_3$ with thermally stable {001} facets [50]. Besides main β - Bi_2O_3 phase, they also observed a small amount of $\text{Bi}_{2.33}$ during calcining $\text{Bi}_2\text{O}_2\text{CO}_3$ at 420 °C. Same experimental results were also found in our experiments if the precursor with high molar ratio (more than 20:5) of $\text{Bi}(\text{OHC}_2\text{O}_4)\cdot 2\text{H}_2\text{O}$: $\text{Bi}(\text{NO}_3)_3$ at 350 °C was calcined. Based on Zhou's and our results, it was speculated that $\text{Bi}_2\text{O}_2\text{CO}_3$ can be translated into $\text{Bi}_{2.33}$ with slow reactive rate, and the main calcined product is β - Bi_2O_3 . However, under the reducing atmosphere (CO from the decomposing of $\text{Bi}(\text{OHC}_2\text{O}_4)\cdot 2\text{H}_2\text{O}$), $\text{Bi}_2\text{O}_2\text{CO}_3$ can be quickly and completely translated into $\text{Bi}_{2.33}$. Of course, there are probably other reasons affecting the decomposition of $\text{Bi}_2\text{O}_2\text{CO}_3$ to $\text{Bi}_{2.33}$, which needs to be further researched.

3.3. Photocatalytic activity test

The photocatalytic activity of S1–S3, $\text{Bi}_{2.33}$ and Bi_2O_3 samples were evaluated by degradation of MO (30 mg/L) dye in aqueous solution under visible light irradiation. As shown in Fig. 5a, S2 sample displays the highest photocatalytic activity among all the photocatalysts, and 100% of MO molecules can be completely decoloured in 60 min under visible light irradiation (Fig. 5b). Compared with the reported Bi-based photocatalysts with the similar photocatalytic condition, S2 sample shows excellent photocatalytic activity [34–40]. This enhanced photocatalytic activity is ascribed to the formation of many junctions with high interface quality in the S2 sample, which can be seen from the SEM and HRTEM images (Figs. 2, 3). However, for S1 sample, small ultrathin $\text{Bi}_{2.33}$ nanosheets are sporadically patched onto the surface of Bi_2O_3 porous rods due to small loaded- $\text{Bi}_2\text{O}_2\text{CO}_3$ content in the respective precursor, which results in few junctions formed. For S3 sample, dense ultrathin $\text{Bi}_{2.33}$ nanosheets almost cover the Bi_2O_3 porous rods, as observed in Fig. 2c, which decreases the light irradiation on Bi_2O_3 rods and the junction interfaces. This shielding effect of dense $\text{Bi}_{2.33}$ nanosheets coating on the Bi_2O_3 rods reduces the photocatalytic activity of S3 sample.

Bi_2O_3 - $\text{Bi}_{2.33}$ heterojunction exhibits better photocatalytic activity under the solar light irradiation than the visible light irradiation. As shown in Fig. 6a, 30, 40 and 50 mg/L of MO dye all can be degraded completely in 30, 40 and 50 min, respectively, using S2 heterojunction as photocatalyst under solar light irradiation. The photographs of MO solution in inset of Fig. 6b–d further prove these results. Compared with BiOBr - ZnO [41] and BiPO_4 / BiOCl [42], Bi_2O_3 - $\text{Bi}_{2.33}$ heterostructure displays outstanding photocatalytic performance for degrading MO dye under solar light irradiation. The degradation curves of MO (30 mg/L) using S1–S3, $\text{Bi}_{2.33}$ and Bi_2O_3 as photocatalysts are shown in Fig. S4.

The photocatalytic activity of Bi_2O_3 - $\text{Bi}_{2.33}$ heterostructures was further evaluated by degradation phenol in aqueous solution under solar/visible light irradiation. The degradation curve and UV-vis absorptive spectra of phenol are shown in Fig. 7. It is found Bi_2O_3 - $\text{Bi}_{2.33}$ heterostructure displays better photocatalytic activity for phenol than the reported Bi-based photocatalysts with the similar photocatalytic condition [43–48], and 30 mg/L of phenol can be degraded in the 30/60 min under the solar/visible light irradiation. The degradation curves of phenol (30 mg/L) using S1–S3, $\text{Bi}_{2.33}$ and Bi_2O_3 as photocatalysts under solar/visible light irradiation are shown in Fig. S5. It can be found S2 sample exhibits the best photocatalytic activity among all the products.

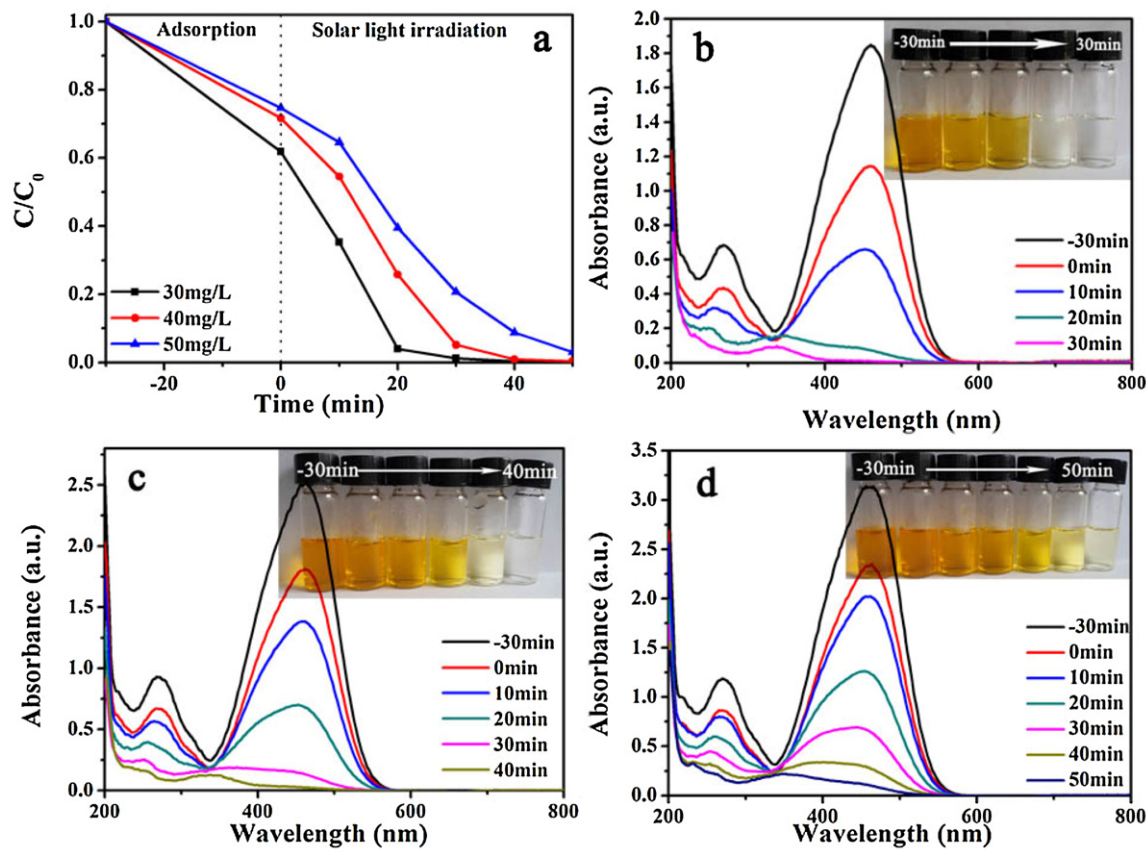


Fig. 6. (a) The degradation curves of MO and (b-d) the respective UV-vis absorption spectra of MO with different concentrations using S2 as photocatalyst under solar light irradiation.

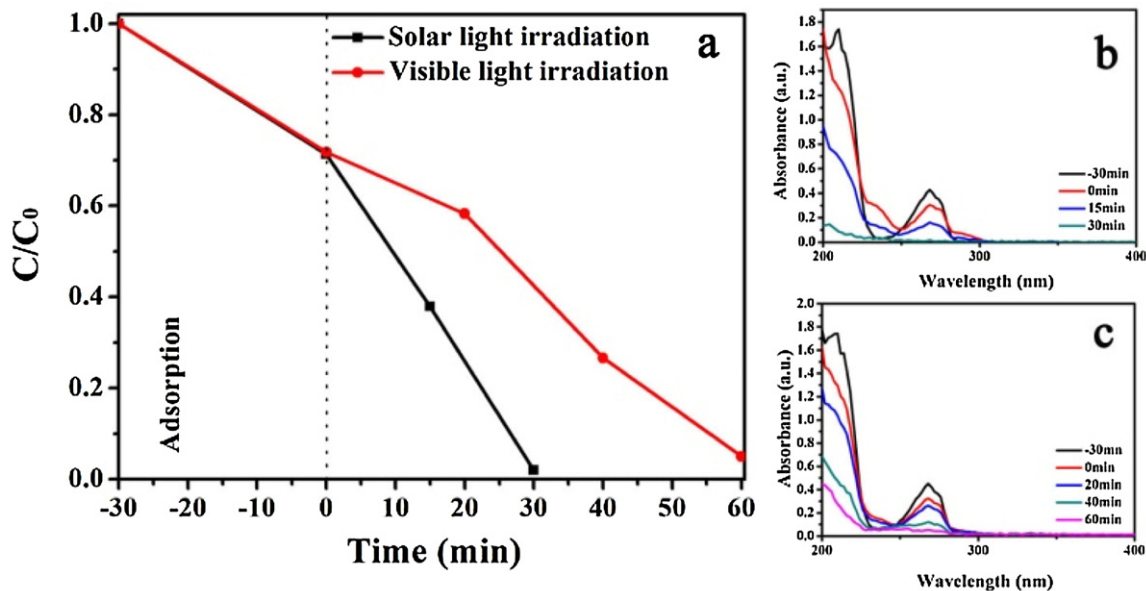


Fig. 7. The degradation curves of phenol (a) and the UV-vis absorption spectra of phenol under solar (b) and (c) visible light irradiation using S2 as photocatalyst.

The degree of photocatalytic mineralization of phenol and MO was tested with TOC analyzer, and the TOC removal efficiency is shown in Fig. 8. It can be seen that the mineralization yield of MO and phenol reaches 100% and 98% in 30 min under solar light irradiation, and 100% and 95% in 60 min under the visible light irradiation

respectively, which confirms that the pollutants are mineralized completely to CO_2 by photocatalysis.

In order to evaluate the stability of $\text{Bi}_2\text{O}_3\text{-Bi}_2\text{O}_{2.33}$ heterostructure during photocatalysis process under solar light irradiation, the S2 sample was used to degrade MO (30 mg/L) dye in five repeated cycles, and the results were shown in Fig. 9. It is noteworthy that

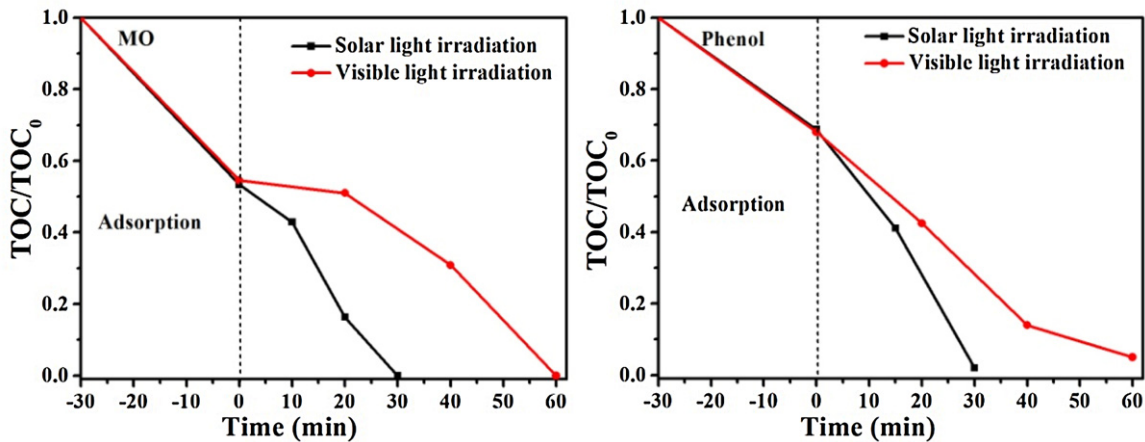


Fig. 8. TOC removal efficiency of MO and phenol using S2 as photocatalyst under solar/visible light irradiation.

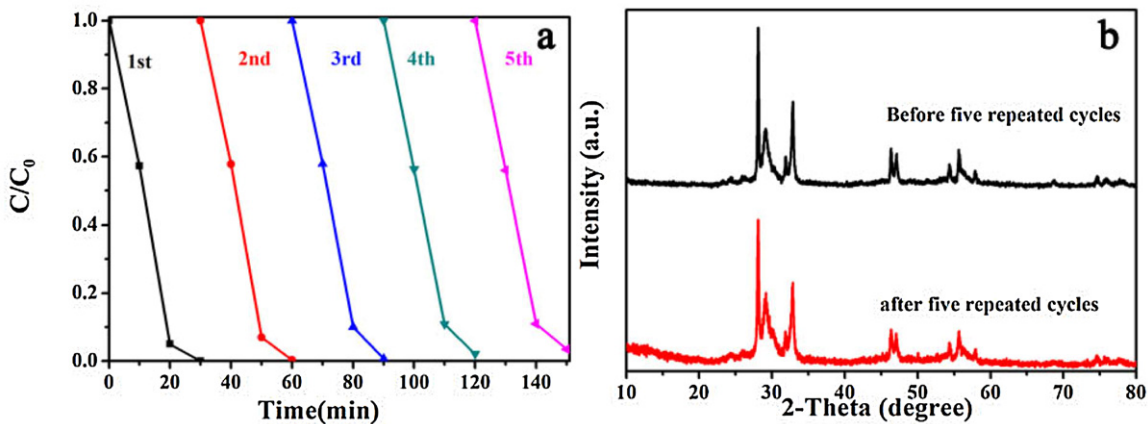


Fig. 9. (a) Cycling times of the photocatalytic degradation of MO in the presence of S2 under solar light irradiation, (b) the XRD pattern of the S2 after five repeated cycles.

S2 sample exhibits good photostability (Fig. 9a), and its photocatalytic efficiency reduces only 2% after five repeated cycles. From the XRD pattern (Fig. 9b), it can be found that the S2 structure has no obvious change after recycled photocatalysis.

3.4. Light absorption and energy band structures

The optical absorption property of the semiconductor is one of the important factors determining its photocatalytic performance. The UV-vis absorption spectra of the obtained samples are displayed in Fig. 10a. The absorption edges of Bi_2O_3 and $\text{Bi}_2\text{O}_{2.33}$ are about 540 nm and 490 nm, respectively. Meanwhile, it is found that the absorption edges of Bi_2O_3 - $\text{Bi}_2\text{O}_{2.33}$ heterostructures shift gradually from 540 to 490 nm with the increase of loaded- $\text{Bi}_2\text{O}_{2.33}$ content, which is due to the sharper visible light absorptive range of $\text{Bi}_2\text{O}_{2.33}$ than Bi_2O_3 . The color of the as-made samples (photographs inset in Fig. 10a) changes from dark yellow (S1) to light yellow ($\text{Bi}_2\text{O}_{2.33}$), which is consistent with the results of UV-vis diffuse reflectance spectra.

The optical band gap of Bi_2O_3 and $\text{Bi}_2\text{O}_{2.33}$ can be determined by the following equation [51]:

$$\alpha h\nu = A(h\nu - Eg)^{n/2}$$

in which α , h , ν , A and Eg are the absorption coefficient, Planck constant, light frequency, a constant and band gap, respectively. And n equals to 4 for indirect band gap and 1 for direct band gap. Here $n=4$ for Bi_2O_3 and $\text{Bi}_2\text{O}_{2.33}$. Fig. 10b gives out the plots of $(\alpha h\nu)^{1/2}$ versus $h\nu$ of Bi_2O_3 and $\text{Bi}_2\text{O}_{2.33}$ [52]. The band gap (ΔEg)

is estimated by extrapolating the straight line to the abscissa axis. So, ΔEg (Bi_2O_3) and ΔEg ($\text{Bi}_2\text{O}_{2.33}$) are estimated to be 2.30 eV and 2.54 eV, respectively.

Trapping experiments were performed to detect the active species generated in the photodegradation process. *Tert*-butyl alcohol (TBA), ammonium oxalate (AO) and 1,4-benzoquinone (BQ) were used as scavengers to trap hydroxyl radicals ($\cdot\text{OH}$), hole (h^+) and superoxide radicals ($\cdot\text{O}_2^-$). It can be observed from Fig. 11 that the photocatalytic degradation of MO and phenol molecules is remarkably inhibited with the addition of AO and BQ. However, the addition of TBA does not cause significant deactivation of S2 photocatalyst, illustrating that $\cdot\text{OH}$ had little contribution to MO and phenol photodegradation. These results demonstrate that $\cdot\text{O}_2^-$ and h^+ are the main active species in the photocatalytic process under solar light irradiation.

To determine the relative positions of conduction band (CB) and VB edges, the total densities of states of VB for Bi_2O_3 and $\text{Bi}_2\text{O}_{2.33}$ were measured, as shown in Fig. 12. The VB edges of Bi_2O_3 and $\text{Bi}_2\text{O}_{2.33}$ are 1.33 and 1.64 eV, respectively. According to the VB edges, combined with band gap of Bi_2O_3 (2.30 eV) and $\text{Bi}_2\text{O}_{2.33}$ (2.54 eV), the CB edge potential of Bi_2O_3 and $\text{Bi}_2\text{O}_{2.33}$ is -0.97 and -0.90 eV, respectively, calculated from the equation of $E_{\text{CB}} = E_{\text{VB}} - Eg$.

Based on the above results and analysis, the degradation mechanism of Bi_2O_3 - $\text{Bi}_2\text{O}_{2.33}$ heterostructures under solar/visible light irradiation was illustrated in Fig. 13. Bi_2O_3 and $\text{Bi}_2\text{O}_{2.33}$ are in contact to form type-II heterostructure according to their positions of CB and VB. The difference of CB and VB positions between Bi_2O_3

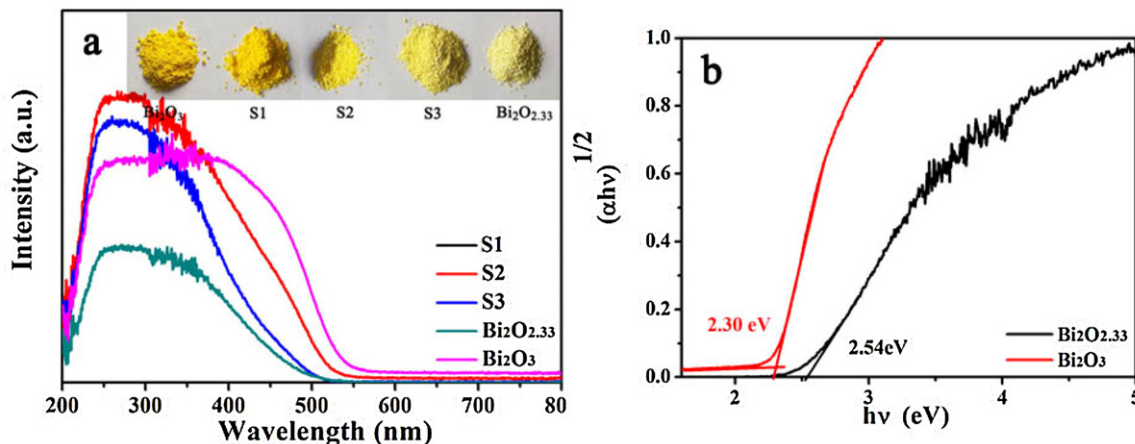


Fig. 10. (a) UV-vis diffuse reflectance spectra of Bi₂O₃, Bi₂O_{2.33} and Bi₂O₃-Bi₂O_{2.33} heterostructures, (b) the plots of $(\alpha h v)^{1/2}$ vs $h v$. (For interpretation of the references to colour in the text, the reader is referred to the web version of this article.)

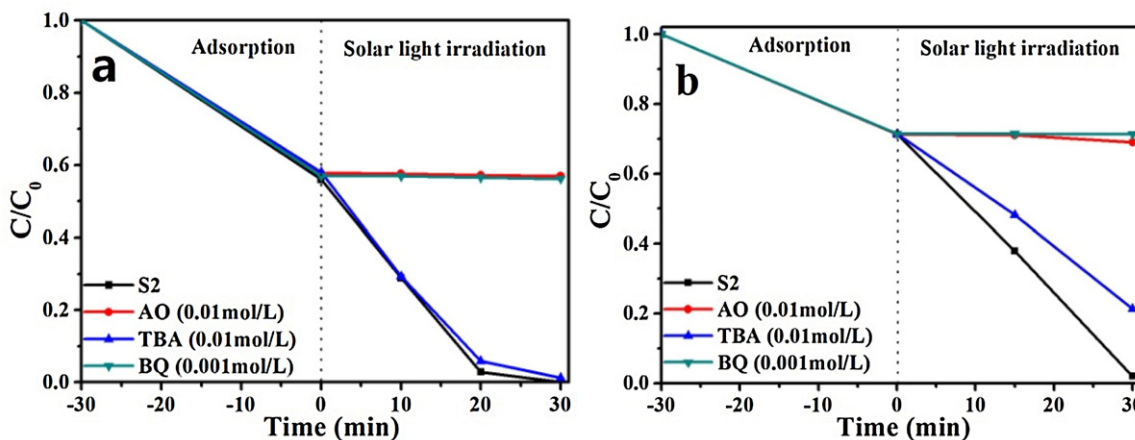


Fig. 11. Active species trapping experiments during the photocatalytic degradation to MO (30 mg/L) (a) and phenol (30 mg/L) (b) under solar light irradiation using S2 as photocatalyst.

and Bi₂O_{2.33} will promote the photogenerated electrons and holes to facilely move in opposite directions, resulting in their efficient separation before recombination. The formation of high quality interface between Bi₂O₃-Bi₂O_{2.33} is an important factor to accelerate electrons and holes transfer. Moreover, 1D Bi₂O₃-Bi₂O_{2.33} nanostructures also offer a direct pathway for charge transport owing to the high surface to volume ratio.

It is well known that many factors would influence the photocatalytic activity of a photocatalyst such as BET surface area and particle size. The prepared Bi₂O₃-Bi₂O_{2.33} (S2) heterostructure has a larger BET surface area than that of pure Bi₂O₃ and Bi₂O_{2.33}, so its photocatalytic activity is much better than that of them. This result shows that the BET surface area is one reason to enhance the photocatalytic activity of S2 sample. On the other hand, however, compared with Bi-based heterostructures photocatalysts with large BET surface area [36,53,54], our prepared Bi₂O₃-Bi₂O_{2.33} exhibits outstanding photocatalytic activity to degrade MO and phenol. This implies the formation of high quality interface is the main reason to increase S2 photocatalytic performance.

According to Fig. 13, it can be found that the CB potential (-0.90 eV) of Bi₂O_{2.33} is enough negative to E^0 ($O_2/•O_2^-$) (-0.046 eV vs NHE) [55], and the electrons in the CB of Bi₂O_{2.33} can reduce O_2 adsorbed on the surface of Bi₂O_{2.33} nanorods to $•O_2^-$ through one electron reducing reaction [56]. The oxidation potential of Bi₂O₃ is 1.33 eV, which indicates that the photogenerated

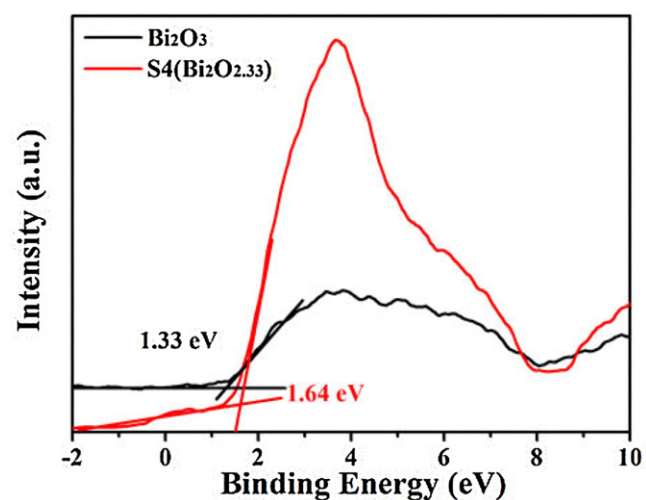


Fig. 12. VB-XPS spectra of Bi₂O₃ and Bi₂O_{2.33}.

holes cannot directly oxidize hydroxyl groups or water molecules adsorbed on the surface of Bi₂O₃ to generate $•OH$ radicals (2.7 V vs NHE). Hence, the h^+ and $•O_2^-$ radicals rather than $•OH$ are the main active species and react directly with MO or phenol in the solution for efficient degradation.

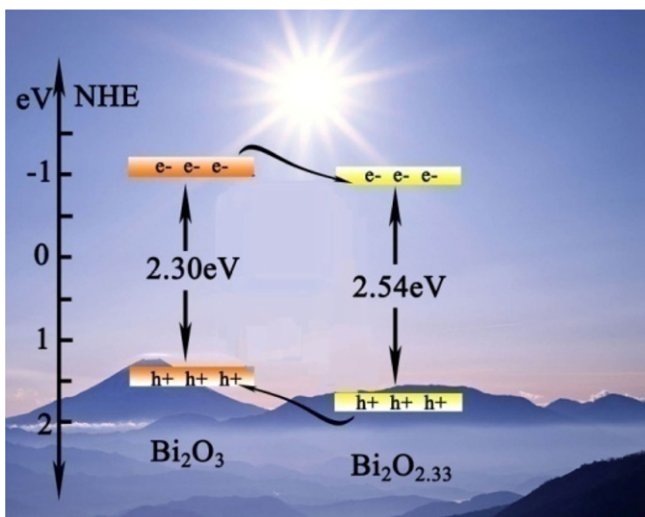


Fig. 13. Schematic diagram of photocatalytic mechanism of Bi_2O_3 - $\text{Bi}_2\text{O}_{2.33}$ heterojunction.

4. Conclusions

In summary, the novel one-dimensional Bi_2O_3 - $\text{Bi}_2\text{O}_{2.33}$ heterostructures with high interface quality have been prepared for the first time. $\text{Bi}_2\text{O}_{2.33}$ ultrathin nanosheets uniformly patched on the surface of the Bi_2O_3 nanorods along radial orientation with well matched lattice fringes. The obtained Bi_2O_3 - $\text{Bi}_2\text{O}_{2.33}$ heterostructures exhibit outstanding photocatalytic performance to degrade phenol and MO dyes with high concentration in short time under solar/visible light irradiation. This superior photocatalytic performance is ascribed to the synergistic effects: (a) formation of junctions enhances the separation of photogenerated carriers; (b) high interface quality provides small penetration barrier for the photogenerated carriers to transfer across the Bi_2O_3 - $\text{Bi}_2\text{O}_{2.33}$ heterojunctions; and (c) one-dimensional ordered nanostructure avails high efficient and directional transport and separation of electrons and holes. This work provides a facile and versatile strategy to fabricate other advanced materials with high interface quality for potential photocatalysis on a large scale.

Acknowledgements

This work is supported by the National Natural Science Foundation of China (21101006) and the Hong Kong Polytechnic University (G-UC35).

Appendix A. Supplementary data

Supplementary data associated with this article can be found, in the online version, at <http://dx.doi.org/10.1016/j.apcatb.2016.11.011>.

References

- [1] C.L. Yu, G. Li, S. Kumar, H. Kawasaki, R.C. Jin, *J. Phys. Chem. Lett.* 4 (2013) 2847–2852.
- [2] C.L. Yu, G. Li, S. Kumar, K. Yang, R.C. Jin, *Adv. Mater.* 26 (2014) 892–898.
- [3] C.L. Yu, W.Q. Zhou, H. Zhu, G. Li, K. Yang, R.C. Jin, *Appl. Catal. B* 184 (2016) 1–11.
- [4] P.A. Sant, P.V. Kamat, *Phys. Chem. Chem. Phys.* 4 (2002) 198–203.
- [5] P.V. Kamat, *J. Phys. Chem. Lett.* 3 (2012) 663–672.
- [6] M.T. Niu, F. Huang, L.F. Cui, P. Huang, Y.L. Yu, Y.S. Wang, *ACS Nano* 4 (2010) 681–688.
- [7] D.F. Zhang, L.D. Sun, C.J. Jia, Z.G. Yan, L.P. You, C.H. Yan, *J. Am. Chem. Soc.* 127 (2005) 13492–13493.
- [8] Y. Ding, P.X. Gao, Z.L. Wang, *J. Am. Chem. Soc.* 126 (2004) 2066–2072.
- [9] X.D. Wang, J.H. Song, P. Li, J.H. Ryou, R.D. Dupuis, C.J. Summers, Z.L. Wang, *J. Am. Chem. Soc.* 127 (2005) 7920–7923.
- [10] Y.S. Jia, S. Shen, D.E. Wang, X. Wang, J.Y. Shi, F. X. Zhang, H.X. Han, C. Li, *J. Mater. Chem. A* 1 (2013) 7905–7912.
- [11] X. Wang, Q. Xu, M.R. Li, S. Shen, X.L. Wang, Y.C. Wang, Z.C. Feng, J.Y. Shi, H.X. Han, C. Li, *Angew. Chem. Int. Ed.* 51 (2012) 13089–13092.
- [12] P. Li, Y. Zhou, Z.Y. Zhao, Q.F. Xu, X.Y. Wang, M. Xiao, Z.G. Zou, *J. Am. Chem. Soc.* 137 (2015) 9547–9550.
- [13] F.T. Li, Q. Wang, J.R. Ran, Y.J. Hao, X.J. Wang, D.S. Zhao, S.Z. Qiao, *Nanoscale* 7 (2015) 1116–1126.
- [14] T.R. Han, Y.J. Chen, G.H. Tian, J.Q. Wang, Z.Y. Ren, W. Zhou, H.G. Fu, *Nanoscale* 7 (2015) 15924–15934.
- [15] I. Robel, M. Kuno, P.V. Kamat, *J. Am. Chem. Soc.* 129 (2007) 4136–4137.
- [16] Z. Dai, F. Qin, H.P. Zhao, F. Tian, Y.L. Liu, R. Chen, *Nanoscale* 7 (2015) 11991–11999.
- [17] Y.F. Yu, Z.H. Ren, M. Li, S.Y. Gong, S.M. Yin, S. Jiang, X. Li, X. Wei, G. Xu, G. Shen, G.R. Han, *CrystEngComm* 17 (2015) 1024–1029.
- [18] B. Jiang, S. Zhang, X. Guo, B. Jin, Y. Tian, *Appl. Surf. Sci.* 255 (2009) 5975–5978.
- [19] L. Li, X. Liu, Y. Zhang, N.T. Nuhfer, K. Barmak, P.A. Salvador, G.S. Rohrer, *ACS Appl. Mater. Interfaces* 5 (2013) 5064–5071.
- [20] X. Zong, H. Yan, G. Wu, G. Ma, F. Wen, L. Wang, C. Li, *J. Am. Chem. Soc.* 130 (2008) 7176–7177.
- [21] X. Zong, G. Wu, H. Yan, G. Ma, J. Shi, F. Wen, L. Wang, C. Li, *J. Phys. Chem. C* 114 (2010) 1963–1968.
- [22] B. Ma, J. Yang, H. Han, J. Wang, X. Zhang, C. Li, *J. Phys. Chem. C* 114 (2010) 12818–12822.
- [23] Y.Y. Sun, W.Z. Wang, L. Zhang, Z.J. Zhang, *Chem. Eng. J.* 211–212 (2012) 161–167.
- [24] D. Yang, H. Liu, Z. Zheng, Y. Yuan, J.C. Zhao, E.R. Waclawik, X. Ke, H. Zhu, *J. Am. Chem. Soc.* 131 (2009) 17885–17893.
- [25] S. Usai, S. Obregón, A.I. Becerro, G. Colón, *J. Phys. Chem. C* 117 (2013) 24479–24484.
- [26] J. Zhang, Q. Xu, Z.C. Feng, M.J. Li, C. Li, *Angew. Chem. Int. Ed.* 47 (2008) 1766–1769.
- [27] Y.Q. Kong, H.G. Sun, X. Zhao, B.Y. Gao, W.L. Fan, *Appl. Catal. A: Gen.* 505 (2015) 447–455.
- [28] A.A. Zavalova, R.M. Imamov, *J. Struct. Chem.* 13 (1972) 811–814.
- [29] G.L. Fang, G. Chen, J.Q. Liu, X. Wang, *J. Phys. Chem. C* 114 (2010) 864–867.
- [30] X.J. Huang, J. Yan, F.L. Zeng, X.L. Yuan, W.J. Zou, D.S. Yuan, *Mater. Lett.* 90 (2013) 90–92.
- [31] H.M. Guan, X.D. Zhang, Y. Xie, *J. Phys. Chem. C* 118 (2014) 27170–27174.
- [32] X.J. Wang, A.L. Zhu, Z.Y. Li, Z.J. Liu, *RSC Adv.* 6 (2016) 25409–25415.
- [33] S.W. Liu, S.H. Kang, H.M. Wang, G.Z. Wang, H.J. Zhao, W.P. Cai, *Chem. Eng. J.* 289 (2016) 219–230.
- [34] Y.C. Huang, W.J. Fan, B. Long, H.B. Li, F.Y. Zhao, Z.L. Liu, Y.X. Tong, H.B. Ji, *Appl. Catal. B: Environ.* 185 (2016) 68–76.
- [35] X.G. Sun, Y.Y. Zhang, C.M. Li, Z.F. Zhang, Z. Peng, H.Y. Si, J.M. Zhang, Y.T. Li, *J. Alloy Compd.* 638 (2015) 254–260.
- [36] A. Etogo, E. Hu, C.M. Zhou, Y.J. Zhong, Y. Hu, Z.L. Hong, *J. Mater. Chem. A* 3 (2015) 22413–22420.
- [37] B. Long, Y.C. Huang, H.B. Li, F.Y. Zhao, Z.B. Rui, Z.L. Liu, Y.X. Tong, H.B. Ji, *Ind. Eng. Chem. Res.* 54 (2015) 12788–12794.
- [38] R. Qiao, M.M. Mao, E.L. Hu, Y.J. Zhong, J.Q. Ning, Y. Hu, *Inorg. Chem.* 54 (2015) 9033–9039.
- [39] X.C. Zhang, B.Q. Lu, R. Li, X.L. Li, X.Y. Gao, C.M. Fan, *Sep. Purif. Technol.* 154 (2015) 68–75.
- [40] J.W. Feng, H.W. Huang, S.X. Yu, F. Dong, Y.H. Zhang, *Phys. Chem. Chem. Phys.* 18 (2016) 7851–7859.
- [41] S.S. Yi, F. Zhao, X.Z. Yue, D.J. Wang, Y.H. Lin, *New J. Chem.* 39 (2015) 6659–6666.
- [42] F.F. Duo, Y.W. Wang, X.M. Mao, X.C. Zhang, Y.F. Wang, C.M. Fan, *Appl. Surf. Sci.* 340 (2015) 35–42.
- [43] X. Xiao, W.D. Zhang, *RSC Adv.* 1 (2011) 1099–1105.
- [44] Y.C. Huang, B. Long, H.B. Li, M.S. Balogun, Z.B. Rui, Y.X. Tong, H.B. Ji, *Adv. Mater. Interfaces* 2 (2015) 1500249–1500255.
- [45] W.Z. Yin, W.Z. Wang, S.M. Sun, *Catal. Commun.* 11 (2010) 647–650.
- [46] J. Cao, B.Y. Xu, H.L. Lin, S.F. Chen, *Chem. Eng. J.* 228 (2013) 482–488.
- [47] Y.Y. Li, J.S. Wang, H.C. Yao, L.Y. Dang, Z.J. Li, *Catal. Commun.* 12 (2011) 660–664.
- [48] X. Xiao, W.D. Zhang, *J. Mater. Chem.* 20 (2010) 5866–5870.
- [49] Y. Peng, K.K. Wang, P.P. Yu, T. Liu, A.W. Xu, *RSC Adv.* 6 (2016) 42452–42460.
- [50] F. Wang, Z. Zhao, K. Zhang, F. Dong, Y. Zhou, *CrystEngComm* 17 (2015) 6098–6102.
- [51] M.A. Butler, *J. Appl. Phys.* 48 (1977) 1914–1920.
- [52] H.Y. Jiang, J.J. Liu, K. Cheng, W.B. Sun, J. Lin, *J. Phys. Chem. C* 117 (2013) 20029–20036.
- [53] W.J. Shan, Y. Hu, Z.G. Bai, M.M. Zheng, C.H. Wei, *Appl. Catal. B: Environ.* 188 (2016) 1–12.
- [54] X.J. Wang, W.Y. Yang, F.T. Li, J. Zhao, R.H. Liu, S.J. Liu, B. Li, *J. Hazard. Mater.* 292 (2015) 126–136.
- [55] A.J. Bard, R. Parsons, J. Jordan, *Standard Potentials in Aqueous Solution*, Marcel Dekker Inc., New York, 1985.
- [56] J. Sheng, X. Li, Y. Xu, *ACS Catal.* 4 (2014) 732–737.